Int. J. Heat Mass Transfer. Vol. 33, No. 1, pp. 39–53, 1990
Printed in Great Britain

0017–9310/90 $3.00 + 0.00

Microscopic study of coupled heat and mass transport during unidirectional solidification of binary solutions—II. Mass transfer analysis

SOHRAB KOUROSH
Department of Orthopaedic Surgery, The University of Texas Health Science Center at Dallas, Dallas, TX 75235, U.S.A.

and

KENNETH R. DILLER and MICHAEL E. CRAWFORD
Department of Mechanical Engineering and Biomedical Engineering Center, The University of Texas, Austin, TX 78712, U.S.A.

(*Received* 27 *December* 1988 *and in final form* 20 *April* 1989)

Abstract—An experimental study was conducted of coupled heat and mass transfer during unidirectional solidification of a binary solution with solute exclusion. This paper reports microscopic scale measurements of the two-dimensional solute concentration field for a freezing protocol that results in uniform cellular phase interface morphology. Densitometric analysis is used to evaluate solute concentration profiles in spatial and temporal coordinates for both the intercellular space and at the advancing liquid–solid interface along forward and lateral vectors. In conjunction with simultaneous temperature field measurements reported in a companion paper, the magnitude of constitutional supercooling is evaluated and compared with interface stability models available in the current literature.

INTRODUCTION

In an accompanying paper [1], the experimental apparatus and procedures for studying coupled microscopic heat and mass transport phenomena during solution solidification and the resulting heat transport measurements are presented. The work was carried out on a specially designed cryomicroscope stage [2] that enables controlled unidirectional freezing of liquids. In the present investigation a binary solution of water and sodium permanganate, which has thermophysical properties similar to a typical physiological medium, was studied. This test system has been demonstrated previously [3] to be quite useful in the experimental simulation of solidification processes in physiologically representative solutions. Sodium permanganate has a diffusion coefficient in water nearly identical to that of sodium chloride [4] and a similar equilibrium phase diagram [5]. In addition, it has a large absorption coefficient in the visible light spectrum, making it suitable for densitometric analysis of concentration [4, 6]. By varying the initial system chemical composition and the thermal boundary conditions on the stage, the phase interface morphology could be controlled to provide either a planar front or a periodic cellular front, in both cases with a time-varying interfacial velocity. A cellular morphology caused a two-dimensional concentration field due to the combined effects of solute exclusion from the solid phase and diffusion in the liquid phase.

The objective of this paper is to present and analyze multi-dimensional concentration field data for a given interface morphology as obtained with this novel apparatus. The pertinent temperature data from the heat transfer portion of the experiment are also presented to allow examination of interface stability criteria. Data for other solidification protocols are documented in ref. [3].

EXPERIMENTAL APPARATUS AND ANALYSIS

Cryomicroscopic stage

The low temperature light microscope and its performance characteristics stage for solidification experiments have been described in detail previously [2] and will be discussed only briefly here. The specimen chamber containing the solution is 12 mm square, and has a depth in the direction of the microscope optical path of about 25 μm. The top, bottom, and sides of the chamber were fabricated of temperature low-conductivity plastic and the two ends of large copper blocks. An array of thermocouples was installed on the bottom surface of the chamber to record the temperature field along the primary heat flow vector. The copper block at the warm end of the chamber was held at ambient temperature, whereas the opposite block was cooled via a refrigerated stream of dry nitrogen gas circulated through an external liquid nitrogen heat exchanger and then an internal flow channel. The freezing protocol was effected

NOMENCLATURE

$\mathscr{A}$	dimensionless parameter, see equation (17)
c	specific heat [J g^{-1} K^{-1}]
C	concentration [wt%]
$\mathscr{C}$	dimensionless concentration
ΔC	supersaturation [wt%]
d_0	capillarity distance [m]
D	solute diffusion coefficient [m^2 s^{-1}]
$f(\mathscr{P})$	functional of $\mathscr{P}$, Péclet number
G	solute or temperature gradient [wt% m^{-1} or K m^{-1}]
$\mathscr{G}$	generalized temperature gradient [K m^{-1}]
$\mathscr{G}$	dimensionless parameter, see equation (18)
h	Mullins–Sekerka stability parameter [K m^{-1}]
k	thermal conductivity [W m^{-1} K^{-1}]
k_B	Boltzmann's constant [J K^{-1}]
K	dimensionless curvature of interface
ℓ	characteristic length [m]
L	latent heat of fusion per unit volume [J m^{-3}]
m	slope of liquidus line on phase diagram [K (wt%)$^{-1}$]
$M(\mathscr{P})$	see equation (20)
$N(\mathscr{P})$	see equation (21)
$\mathscr{P}$	Péclet number, see equation (4)
R	approximate experimental tip radius
ΔS	volumetric entropy of fusion [J m^{-3} K^{-1}]
T	temperature [K]
ΔT	supercooling [K]
ΔT_0	freezing range of a solution [K]
v	atomic volume [m^3]
V	velocity [m s^{-1}]
y	coordinate position normal to the primary growth direction of the interface
y	dimensionless position normal to the primary growth direction of the interface.

Greek symbols

α	thermal diffusivity [m^2 s^{-1}]
γ	surface tension, or free energy [J m^{-2}]
κ	partition coefficient
λ	interface perturbation wavelength [m]
Λ	diffusion mixing length [m]
ρ	tip radius of curvature [m]
σ	stability parameter
τ	dimensionless time.

Subscripts

c	capillarity
e	equilibrium
h	heat
if	interface
l	liquid
m	melting
pd	phase diagram
s	solid
t	tip
u	solute
∞	far-field state.

by a microprocessor-based proportional temperature controller [7]. The input signal was obtained from a thermocouple mounted at the interface between the cold block and the specimen chamber. The electric resistance heater was integral to the cold block so as to balance the magnitudes of simultaneous heating and cooling. This method enabled the rate of temperature change to be regulated independent of absolute temperature.

Examination of the thermal field has shown it to be one-dimensional within small tolerances. This was confirmed by the uniformity of the phase interface in the spanwise direction. The thinness of the chamber along the optical axis, 25 μm, plus the presence of integral insulating layers above and below, act to minimize three-dimensional effects at the interface, as verified under many operating conditions by scanning the microscope focal plane vertically through the specimen during freezing.

Data acquisition

The arrangement of apparatus components that comprise the experimental facility are depicted in Fig. 1. The temperature data were acquired simultaneously with the mass concentration data via combined video microscopy and thermocouple monitoring. Temperature readout from an array of sensors was performed typically at 6 s intervals over the duration of an experiment that could last as long as 1 h or more. The concentration information was extracted from a series of micrographs obtained by computer processing of recorded video camera data. During an experiment, the solid–liquid interface was kept in the center of the microscopic field of view by traversing the stage at the same speed but in the opposite direction to the interface motion. Interface position was recorded directly from a position sensor mounted on the moving stage.

The microscope optics were set up for a total magnification of 125 power, and the image was diverted by a beam splitter to incorporate both 35 mm camera photography and video camera recording. The video system was equipped with a digital time/date generator so that temporal data could be superimposed onto the visual record with ± 0.1 s accuracy. Serial images were digitized on a Colorado Video CVI 274

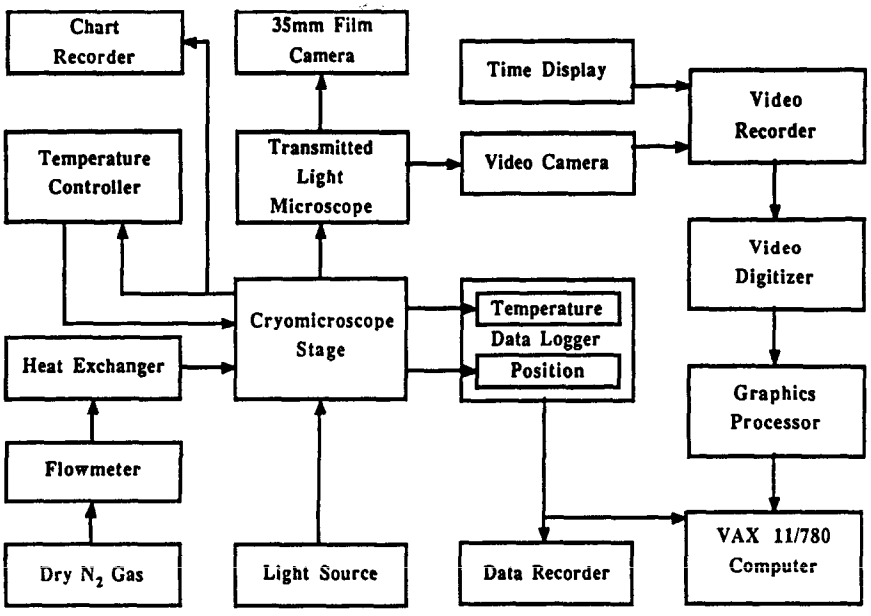

FIG. 1. Functional arrangement of the apparatus components for performing digital densitometry of aqueous solutions frozen on a light cryomicroscope stage to measure the two-dimensional transient solute concentration fields.

frame grabber and two-dimensional densitometric analysis was performed on a Grinell GMR-270 interactive color graphics and image processing system coupled with a VAX 11/780 computer.

Concentration measurement

Micrographs were digitized and stored as a two-dimensional array of 512 by 512 pixels, with eight bits of gray level information ranging from 0 to 255. For contour plotting the image was reduced to a 102 by 102 array by simple averaging of adjacent five pixel blocks resulting in a reduction in random electronic signal noise. The data was presented as a plot of isointensity contours, which were then converted to isoconcentration contours based on calibration trials. This data reduction procedure was also used to perform a qualitative analysis of the phase front morphology.

The optical system was calibrated to convert densitometric measurements of gray level intensity into values of solute concentration. Calibration experiments were performed on control specimens of uniform thickness (equal to that of the freezing chamber) sodium permanganate solutions varying from zero to approximately the eutectic composition of 41.4 wt% [5]. The micrographs were digitized and the resulting mean intensities determined over the entire image. The values were then used to create the gray level vs solute concentration curve shown in Fig. 2. The curve demonstrates an exponential function that resembles the theoretical Beer's law for absorptance and transmittance.

Test solutions were prepared from an initial mixture of about 40 wt%, formed by dissolving $NaMnO_4$ crystals in distilled water and repeated filtering to remove residual solid phase solute. The stock solution was then serially diluted with water to obtain the desired working mixtures. Concentrations of these mixtures were determined by two methods: titration and osmometry. The freezing point depression measurements were performed on an Advanced Instruments model 3R osmometer as the primary means for assessing solution composition, with titration [8] used as a secondary check. In general there was an agreement within 1.1% between the two methods for an operating range of 0–4000 milli-

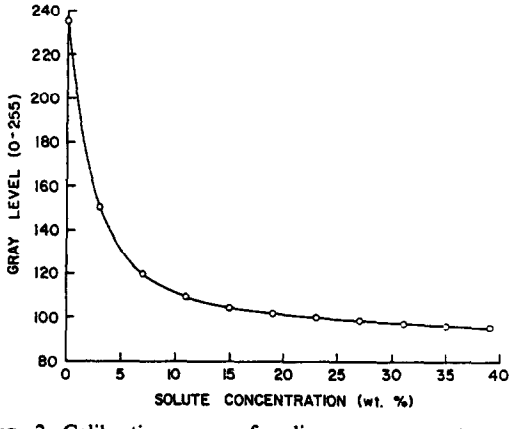

FIG. 2. Calibration curve of sodium permanganate concentration as a function of digitized gray level from video micrographs. The data points were obtained for uniform solutions of incremental solute concentrations suspended in a constant thickness chamber corresponding to that of the cryostage on the light microscope under standard illumination intensity.

osmol for calibration against standard solutions of known composition.

Concentration profiles were measured from the two-dimensional gray level map along vectors both normal and parallel to the direction of phase front growth. The vectors were arranged as a grid comprised of five lines parallel to the growth axis between the cell centerline and the intercellular midline, and five lines extending laterally from the basal plane of the intercellular region to a location well past the cell tips. Morphological parameters of the phase interface were also calculated, including the average cell cross-sectional area, cell length to breadth aspect ratio, cell axis angle, and intercellular spacing. Special computer vision software was developed to isolate the interface and compute many of the morphological parameters [9].

The array forming a network of gray level intensities along given vectors in the image was converted to the equivalent concentration, and a least-squares cubic-spline curve was fit to the data for subsequent analysis. Particular attention was directed toward determination of the transient location of the phase interface, as well as the build-up of a layer of concentrated solute preceding the advancing front. Data from the axial and lateral concentration profiles and gradients were applied to evaluate lateral solute segregation, interface stability, and constitutional supercooling.

Experimental uncertainty in the measured position of the isoconcentration contours is estimated at ± 10 μm. Local concentrations were determined within ± 0.5 wt% in the dilute solution region, which increased to ± 2.5 wt% in the vicinity of the eutectic point.

RESULTS AND DISCUSSION

Solute concentration analysis

Solution solidification experiments were conducted for a wide range of freezing protocols to produce both planar and cellular interface morphologies, from which hundreds of micrographs were prepared for computer analysis. The data selected for processing in the present study were representative of a variety of freezing patterns. The processing sequence applied to derive two-dimensional concentration data from the micrographs is illustrated in this section for a single micrograph that is typical of the data generated on the cryostage. The micrograph is selected from the data set subjected to thermal analysis in the companion paper [1].

The experimental trial was conducted for manipulation of boundary conditions to effect a transition from planar to cellular interface morphology. A digitized micrograph of the phase interface, obtained by digital processing of a video image, is shown in Fig. 3. The micrograph depicts a regular, symmetrical cellular shape that is biased slightly clockwise from the primary growth vector (which is oriented horizontally in the figure). The very thin cross-section of the cryostage and the insulated upper and lower surfaces act to insure that the geometry of the phase front is essentially two-dimensional, with minimal variation in temperature and concentration along the optical axis.

A simple contour fitting algorithm was applied to the two-dimensional gray level map to obtain isointensity patterns at specified intervals. An example of the resulting isoconcentration map is illustrated in Fig. 4. As in a topographical drawing, the density of the contour lines is in direct proportion to the local concentration gradient and also indicates a vector direction of the gradient. The shape of the concentration contours seen in Fig. 4 bears a clear resemblance to the phase interface in Fig. 3. The profiles in Fig. 4 are plotted as lines of constant gray level; however, the contours labeled 100 and 120 represent the region identifiable as the solid–liquid phase change zone. The gray level at the cell tip can be converted to a concentration value of about 7.1 wt% by interpolation of the calibration curve in Fig. 2. The solute concentration in the region ahead of the cell tips decreases to the background level with distance from the interface.

Quantitative analysis of the concentration distribution in two dimensions involved convolving a 5 by 5 grid for pixel averaging onto a defined image area of interest to reduce the spatial resolution of the data. The area was selected to extend from an intracellular center axis to an adjacent parallel intercellular axis, and from the basal plane of the cellular structure to a locus in the melt beyond the region of solute accumulation. Figures 5–7 present intensity and concentration vs position plots along various grid axes for the subject data. Figure 5 is a typical profile of gray level intensity along a vector located midway between two cells in the direction of the interface movement. A least squares cubic-spline curve is fit to the data.

Profiles of solute concentration along parallel vectors passing through intercellular and intracellular midpoints in the direction of the interface growth are shown in Fig. 6. The effect of solute exclusion from the solid phase is seen clearly in the abrupt discontinuity in the concentration along the intracellular profile. The concentration of solute is essentially zero within the solid phase, and shows a near step increase in the boundary region of the liquid melt where rejected solute accumulates. It then decreases to the far-field valve associated with solute diffusion away from the advancing phase front. The intercellular profile shows the distribution of solute in the liquid phase trapped between the adjacent growing ice cells. There is a build-up of solute toward the basal plane. As the temperature decreases more of the water is sequestered into the solid phase and the intercellular liquid solution channel becomes progressively narrower. With advancing position toward the tip region the concentration decreases. Eventually, the intracellular

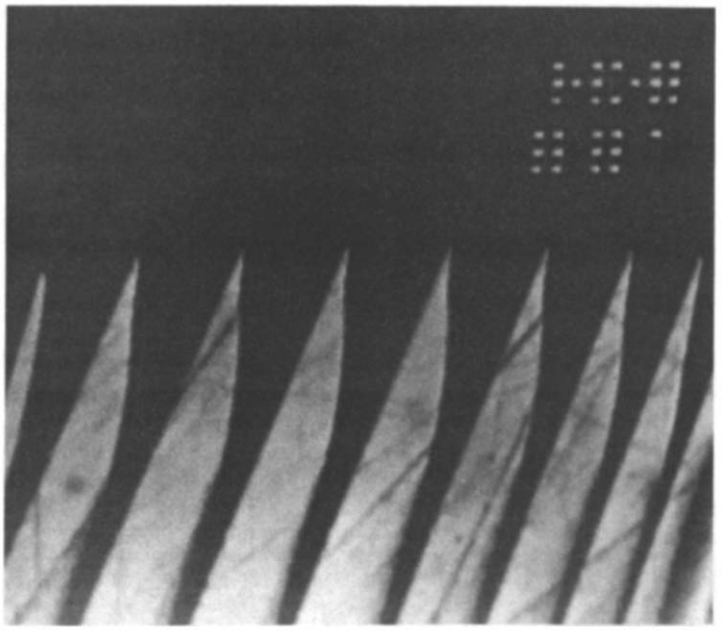

FIG. 3. Digitized micrograph of the phase front of a 2.16% aqueous sodium permanganate binary solution demonstrating a cellular interface morphology. The local solute concentration is indicated by the relative gray level of the image, and can be observed in two dimensions in the region of the interface.

and intercellular profiles become nearly identical at a position equal to a few tip radii ahead of the interface, and then continue to decrease in the far field approaching the initial melt composition.

Lateral concentration data along vectors parallel to the basal plane are presented in Fig. 7. In this figure, the concentration gradient in the intercellular space is quite evident. Data are presented for five positions, with the first three between the basal plane and the tips and the remaining two in the field region. For the intercellular data the concentration is highest along the solid–liquid boundary and it diminishes as the intercellular centerline is approached and then rises again, reflecting the periodic cell spacing and verifying that the solute diffusion process has a significant two-dimensional character. Lines 4 and 5 represent the tip and far-field region where the spanwise gradients in concentration have diminished and the concentration is dropping towards its initial liquid concentration value.

Numerous models for steady-state growth of phase interfaces have been developed in recent years, as summarized by Glicksman *et al.* [10]. A common feature among the theories follows after Ivantsov [11] that a dendrite is assumed to grow as a paraboloid of revolution along its axis, and to maintain an isothermal solid–liquid interface, or surface. For the present experiments, assuming that equilibrium phase change conditions prevail at a steady growth rate, an isothermal surface will be associated with each of the isoconcentration profiles identified in the previous figures. Coupling between the thermal and concentration fields occurs via the liquidus curve on the thermodynamic equilibrium phase diagram for sodium permanganate and water binary solutions, as described in ref. [5]. A solute concentration of 7.1 wt% measured at the leading edge of the phase interface in Figs. 3 and 4 corresponds to a temperature on the liquidus curve of -1.7°C, which is in close agreement with the interface temperature determined by the complementary thermal analysis procedure for the same data set [1].

Supercooling

A number of phenomena may contribute to the development of a temperature at the interface that differs from the equilibrium phase change value of the melt at the initial uniform composition, which is often described in terms of a supercooling effect. Coupling between the heat and mass transfers is related not only to the temperature and solute concentration relationships defined by the thermodynamic phase diagram, but also is involved with dimensions and morphology of the growing boundary between the solid and liquid phases. Experimental protocols provide specific data describing these three classes of parameters (thermal, chemical and morphological), and it is desirable that analysis should present a general description of the data owing to fundamental principles and appropriate kinetic phenomenological relations.

The array of thermocouples embedded in the stage at discrete positions afford a continuous measure of the interface temperature and the temperature gradient during freezing trials. This thermal data, in combination with two-dimensional measurements of the concentration field in the region of the solid–liquid interface, provide the basic data for determination of the degree of supercooling (or *undercooling*, as is often

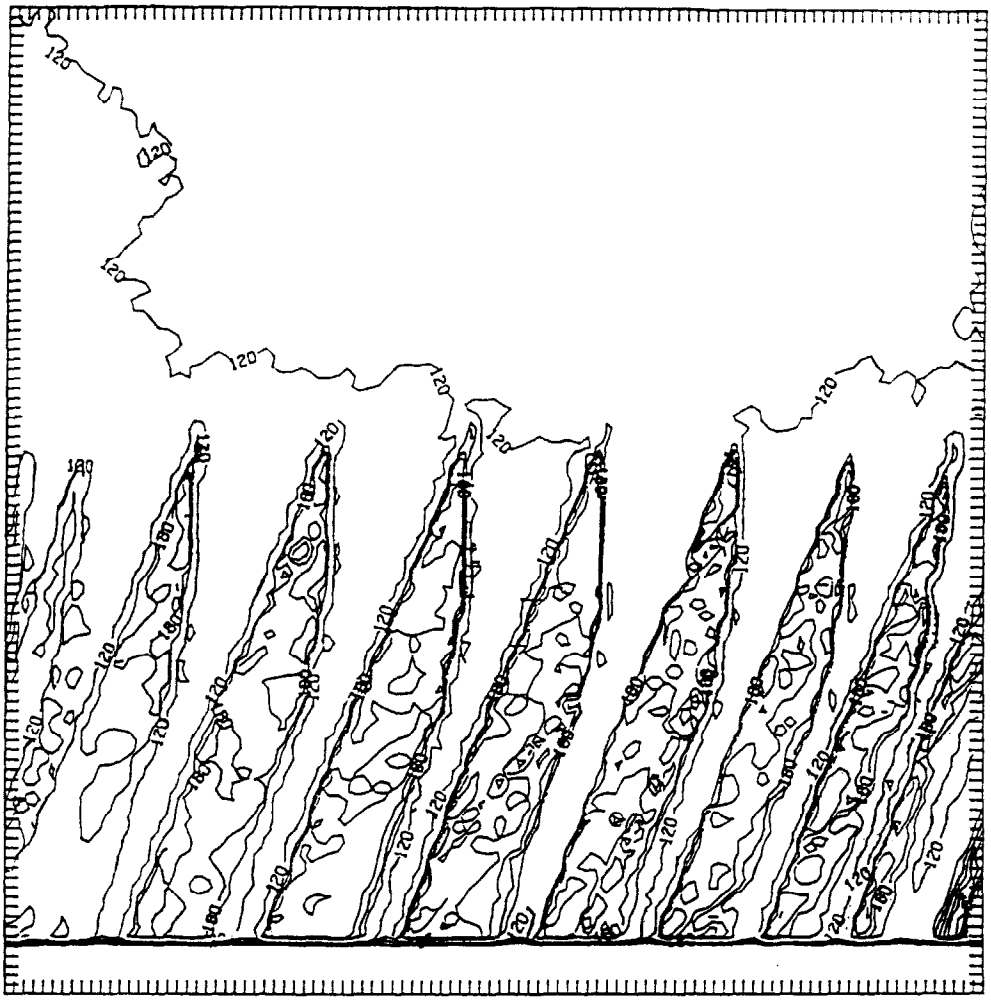

FIG. 4. Isoconcentration contours plotted for the micrograph in Fig. 3 showing the distribution of solute in relation to the phase interface.

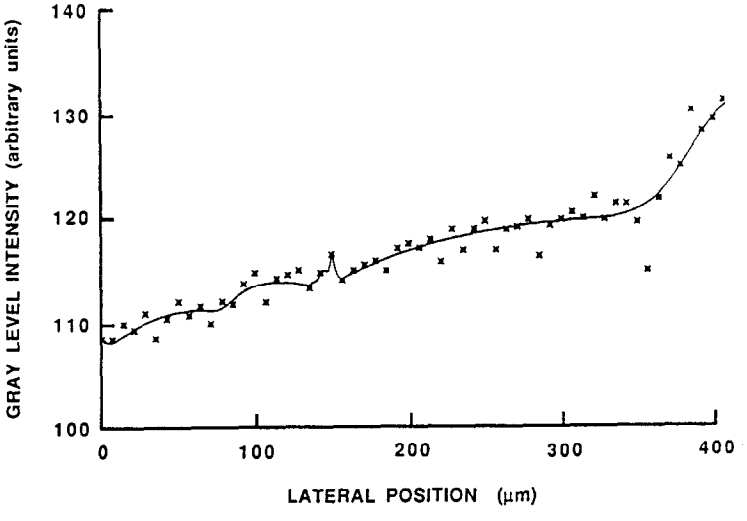

FIG. 5. Plot of the gray level intensity data along an intercellular vector. Higher solute concentrations correspond to lower intensity values due to propositional attenuation of light transmitted through the specimen.

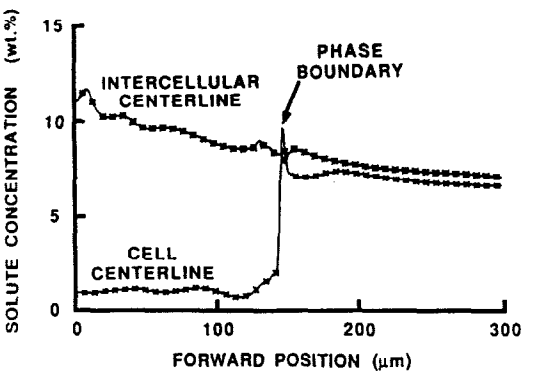

FIG. 6. Solute concentration profiles along vectors lying on the intercellular and intracellular midlines in the direction of interface growth.

used synonymously). Supercooling is defined according to a number of different criteria, depending on the specific phenomenon to be studied. In general the supercooling may be considered as the deviation of the actual solid–liquid interface temperature from that of pure solvent undergoing solidification with a planar interface; it consists of the summation of several different components, including capillary supercooling, kinetic supercooling, and constitutional supercooling, as discussed by Trivedi *et al.* [12, 13]. Thermal and compositional data from the present experiments will be combined to evaluate a number of existing models that describe the interfacial behavior during solidification of binary melts.

Capillary supercooling is defined in terms of the difference between the equilibrium melting temperature of the substance, T_m, and the freezing temperature of its curved interface, T_e, as described by the Gibbs–Thompson equation [12, 14]

$$T_e = T_m - \frac{\gamma K}{\rho(\Delta S)} \tag{1}$$

where K is a dimensionless curvature, i.e. curvature multiplied by the radius of curvature of the interface, ρ the minimum radius of curvature at the advancing interface tip, γ the surface tension, and ΔS the entropy of fusion per unit volume. Measurement of curvature involves the use of procedures such as those adopted by Somboonsuk and Trivedi [15] which are outside the scope of this work. For this reason, T_e cannot be measured accurately by our methods. The value of curvature can, however, be approximated by $1/R$ if the assumption of a spherical shape for the small cell tip region is made [12].

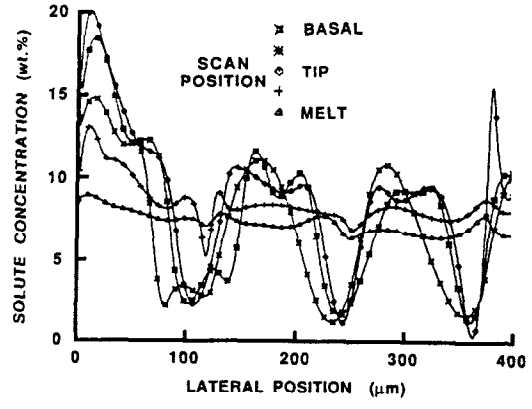

FIG. 7. Solute concentration profiles along lateral vectors in the intercellular space between the basal plane and tip region normal to the direction of interface growth.

Kinetic supercooling is defined simply as the difference between the equilibrium temperature of the interface, T_e, as defined by equation (1), and the actual temperature of the interface, T_{if}.

Constitutional supercooling is the difference between the actual interface temperature, T_{if}, and the temperature equivalent of the interface concentration, as determined from the phase diagram for the melt solution, T_{pd}

$$\Delta T = T_{if} - T_{pd}. \tag{2}$$

This temperature difference can also be used in lieu of the kinetic supercooling because these two values converge when the capillary effects are negligible.

Measurement at the microscopic scale of the dynamic temperature and solute concentration fields near the moving solid–liquid boundary yield data to describe the supercooling effects during freezing, and also lead to the prospect of testing the applicability of theories of interface morphology stability.

Interface stability

The combined thermal and compositional experimental data acquired on the cryomicroscope stage may be subjected to analysis by various published methods, applied to understand and interpret phase interface stability. This data has been reduced and analyzed according to three classic theories, i.e. those of Mullins and Sekerka for a planar interface [16–18], of Trivedi for a dendrite tip [13], and of Langer and Müller-Krumbhaar for the product of interface growth rate and tip radius [19]. Although there exist more detailed and comprehensive stability models than the above that include the effects of morphological anisotropy [20, 21], planar to denritic transition criteria [22–25], selection of interface shape when a planar surface becomes unstable [26–29] and lateral growth phenomena [30, 31], it is the intention in the present analysis to subject this data to evaluation by the earlier and more simple models. Further detailed analyses will be presented subsequently. It is important to compare the actual experimental protocols with the specific inherent to each of the stability models in order to obtain a meaningful interpretation of the evaluation.

The Mullins and Sekerka (M–S) [17] stability criterion for unidirectional solidification of a dilute binary alloy at constant interface velocity predicts that a planar phase front will be stable when

$$\tfrac{1}{2}(\mathcal{G}_s + \mathcal{G}_l) + mG_h < k \tag{3}$$

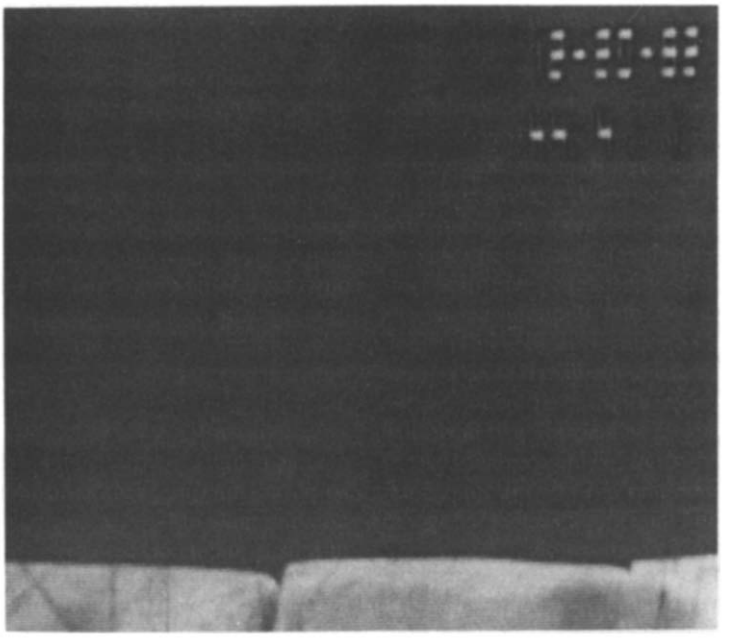

FIG. 8. Quasiplanar phase interface with a small initial morphological instability.

where $\mathscr{G}_s$ and $\mathscr{G}_l$ are generalized temperature gradients in the solid and liquid phases, respectively, as defined by the relationship

$$\mathscr{G}_s = G_s\left(\frac{2k_s}{k_s+k_l}\right) \quad \text{and} \quad \mathscr{G}_l = G_l\left(\frac{2k_l}{k_s+k_l}\right)$$

where $\mathscr{G}_s$ and $\mathscr{G}_l$ are the actual laterally averaged temperature gradients at the interface and k_s and k_l the thermal conductivities in the solid and liquid phases, respectively; G_h is the solute concentration gradient in the melt; m the slope of the liquidus line from the equilibrium phase diagram; and δ a stability parameter which always has a value less than the product of mG_h [18]. The ratio of the equilibrium concentration of solute on the solid side of the interface to that on the liquid side is the solute partition coefficient, κ. In the case of aqueous solutions for which κ equals zero, solute is excluded from the solid phase, and the stability parameter, δ, also goes to zero.

Figure 8 shows an example of an interface that is essentially planar, taken in sequence during the experiment. Figures 9 and 10, taken further into the experiment, depict respectively a planar interface at the onset of instability and after an unstable morphology has become established. Appropriate parameter values from the experimental data for these three micrographs, including the temperature gradients in the solid and liquid phase and the concentration gradient at the interface, were substituted into equation (3) to calculate corresponding values of the M–S criterion. The results of these computations are present in Table 1. As the apparent tendency toward instability increases progressively in the sequence of micrographs in Figs. 8–10, the sum of the two terms in equation (3) likewise also increases. Figure 8 nominally satisfies the M–S stability criterion, indicative of the phase front having approximately planar morphology. Figure 9 shows a noticeable perturbation from planarity, and Fig. 10 is obviously highly unstable, which are in agreement with the large values of equation (3). Although the experimental conditions do not exactly match the assumption of constant interface velocity on which the M–S criterion is based, there is nonetheless a clear quantitative agreement between the theory and experiment.

Langer and Müller-Krumbhaar (L–MK) have presented a theory of dendritic growth in which the boundary velocity and geometry of a free dendrite is governed by a stability criterion [19, 32, 33]. It is assumed that either a thermal or a chemical diffusion process controls the growth process, and that transport of mass and heat in the solid phase are negligible. Stability of the interface is described in terms of two dimensionless parameters, defined as follows. The Péclet number is

$$\mathscr{P} = \frac{\rho}{\ell} \tag{4}$$

where ρ is the tip radius of curvature; ℓ a diffusion length for either solute or heat transport, given by

$$\ell_c = \frac{2D_l}{V} \quad \text{and} \quad \ell_h = \frac{2\chi_l}{V} \tag{5}$$

where D_l is the chemical (solute) diffusion coefficient, χ_l the thermal diffusivity, and V the interface velocity.

A stability parameter, σ, is defined as

$$\sigma = \frac{\ell d_0}{\rho^2} \tag{6}$$

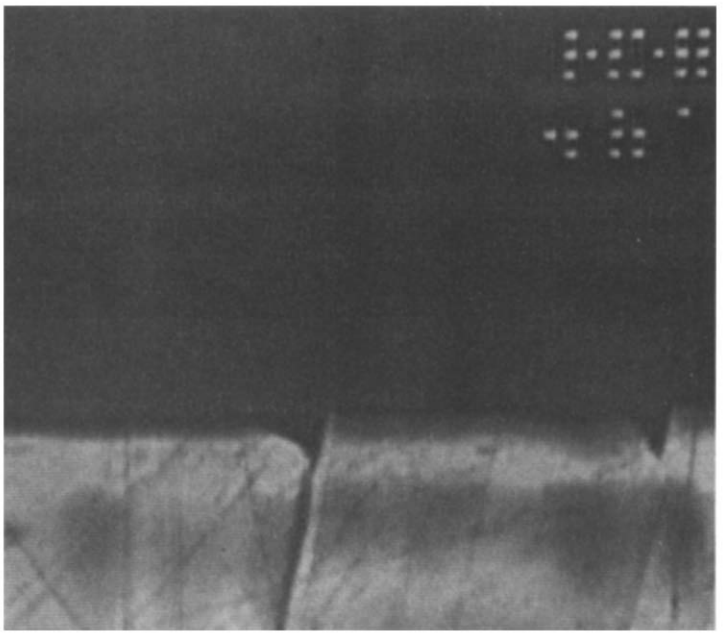

FIG. 9. Quasiplanar phase interface with a progressively growing morphological instability.

where d_0 is a capillary distance for either thermal or chemical phenomena

$$d_{0,c} = \frac{\gamma v C_e}{(\Delta C) k_B T_m} \quad (7)$$

$$d_{0,t} = \frac{\gamma T_m}{L(\Delta T)} \quad (8)$$

where γ is surface tension; v the atomic volume; C_e the equilibrium concentration of the solution at the phase interface; ΔC the supersaturation; k_B the Boltzmann constant; and L the latent heat of fusion per unit volume. T_m is defined for use in equation (1) and ΔT is defined for use in equation (2).

The M–S stability criterion can also be expressed [19], in terms of the shortest wavelength of a perturbation, λ, that would cause a plane interface mov-

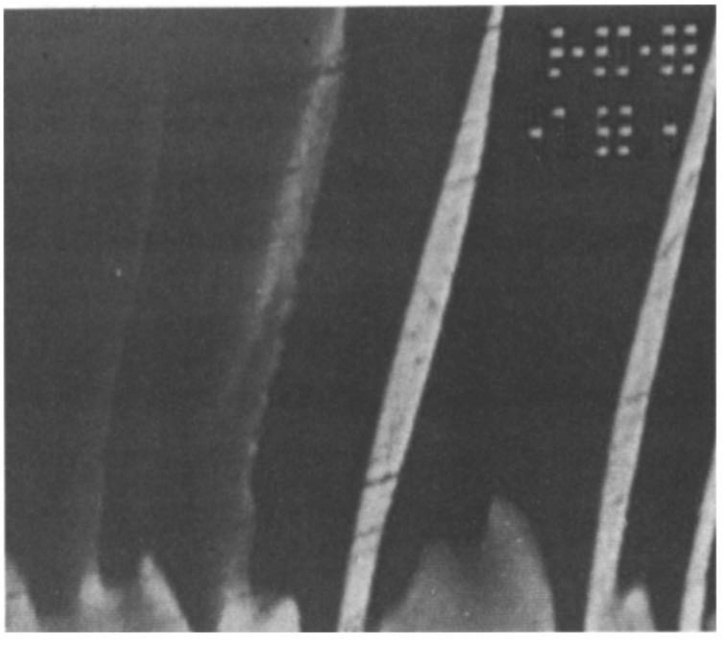

FIG. 10. Boundary morphology of an unstable solid–liquid phase interface.

Table 1. Mullins Sekerka interface stability criteria parameters from equation (3) for the thermal and composition data of the micrographs in Figs. 8–10

Fig. No.	G_S (°C cm^{-1})	G_L (°C cm^{-1})	$\mathscr{G}_s$ (°C cm^{-1})	$\mathscr{G}_l$ (°C cm^{-1})	$-(\mathscr{G}_s+\mathscr{G}_l)/2$ (°C cm^{-1})	m (°C (wt%)$^{-1}$)	G_c (wt% cm^{-1})	Sum (°C cm^{-1})
8	31.27	29.40	49.17	12.56	−30.86	0.278	120	2.50
9	34.83	30.79	54.77	13.15	−33.96	0.298	190	22.66
10	38.19	32.66	60.06	13.95	37.00	0.311	270	46.90

ing at velocity V, to become unstable. This is expressed as the dimensionless ratio

$$\sigma = \left(\frac{\lambda}{2\pi\rho}\right)^2 \tag{9}$$

where $\lambda = 2\pi\sqrt{(\ell d_0)}$.

With the stability criterion of the form $\lambda \equiv \rho$, given by L–MK [19, 33], equation (6) becomes

$$\sigma = \frac{2Dd_0}{V\rho^2} = \sigma^* \tag{10}$$

where L–MK find that the constant $\sigma^* \cong 0.025$ is the approximate operating point for stable growth of a dendrite. Although the evaluation of σ^* remains uncertain within approximately 20%, equation (10) should provide a general description for the growth velocity of dendrites irrespective of the system or material.

The values of σ^* were calculated for 17 cases of steady and non-steady cellular interfaces, based on the physical properties of this experimental system as given in ref. [1] and do not agree with the given value of σ^* in equation (10). In fact they are several orders of magnitude larger than 0.025. One possible cause might be the fact that the value of $1/R$ was used for the radius of curvature. R is the tip radius of a dendrite approximated by a circle. Another possible reason is the procedure for measurement of velocity, which for the experimental verification of the above mentioned theory, was carried out with supercooled liquid in a capillary tube.

The sensitivity of the calculation for σ^* to the value of radius of curvature, and the fact that the calculation of this value as cited in the literature is somewhat subjective should also be considered. The lack of agreement between the model and the present experimental data may be attributable in part to the limiting assumptions employed by Langer and Müller-Krumbhaar [19]. The L–MK value of σ^* was obtained from a calculation in which the heat flow in the solid was neglected completely and was based on experiments for the solidification of succinonitrile, for which the thermal diffusivity of the solid and liquid phases are roughly equal. This is far from the case of aqueous solutions.

Bower *et al.*, demonstrated that the supercooling, ΔT, at a dendrite tip could be described by the simple relationship [34]

$$\frac{G_l D_l}{V(\Delta T)} = 1 \tag{11}$$

where V is the interface velocity and D_l the solute diffusion coefficient in the liquid. This expression is valid only under the conditions of large G_l and small V, and neglects lateral diffusion of solute in the region of the dendrite that gives rise to the criterion for establishing an appropriate tip radius.

Trivedi has subsequently developed a stability theory of dendritic interface growth which does account for the combined effects of both the heat and mass transfer [13]. A criterion is presented based on relative diffusion lengths for heat and mass transport and interface geometry to identify the conditions for which the dendrite tip is stable so that it can grow at a steady rate. In the limiting case of a planar interface, the stability condition for this analysis becomes

$$\frac{G_l D_l}{V(\Delta T_0)} = 1. \tag{12}$$

For the system under consideration (an aqueous salt solution), as the freezing front moves it can be assumed that all of the solute is rejected from the solid phase. Thus, the partition coefficient $\kappa = 0$. This means that the solvent liquidus line of the phase diagram is vertical and ΔT_0, which is the freezing range of the solution for a specific composition, is not defined for aqueous solutions. Consequently, this criterion is not applicable directly to the present system. Trivedi also confirms the agreement between his experimental results and the L–MK value of σ^*, but his analysis was also carried out on the same chemical system (succinonitrile).

Comparison of C and T data with theoretical models

The results of thermal and concentration analyses are compared with the Trivedi model [13] for cellular dendritic tip temperature and concentration, as given in the following relations. Trivedi's analytic result for tip concentration obtained as a function of various length scales of the process

$$\frac{\kappa(C_l - C_\infty)}{C_\infty(1-\kappa)} = \left(\frac{\phi\kappa}{1-\phi(1-\kappa)}\right) \times \left(1 + \frac{1}{2}\mathscr{G}N(\mathscr{P}) + \frac{2\sigma^*}{\mathscr{P}^2}f(\mathscr{P})\right) \tag{13}$$

and it is extended to the tip temperature using the relationship

$$\frac{\Delta T}{\Delta T_0} \approx \frac{\kappa(C_i - C_\infty)}{C_\infty(1-\kappa)}. \tag{14}$$

In equation (13) $\mathscr{A}$ and $\mathscr{G}$ are ratios of phenomenological dimensions identified at the growing interface for solute diffusion, ℓ_u, defined in equation (5), and two new dimensions: heat diffusion, ℓ_h, and capillarity length, ℓ_c

$$\ell_h = \frac{\kappa(\Delta T_0)}{G_l} \tag{15}$$

$$\ell_c = \frac{\Gamma}{\kappa(\Delta S)(\Delta T_0)}. \tag{16}$$

Thus

$$\mathscr{A} = \frac{\Gamma V}{2\kappa(\Delta S)(\Delta T_0)} = \frac{\ell_c}{\ell_u} \tag{17}$$

$$\mathscr{G} = \frac{2G_{if}D}{\kappa V(\Delta T_0)} = \frac{\ell_u}{\ell_h} \tag{18}$$

where G_{if} is an effective temperature gradient at the interface defined as

$$G_{if} = \frac{k_l G_l N(\mathscr{P}) + k_s G_s M(\mathscr{P})}{k_l N(\mathscr{P}) + k_s M(\mathscr{P})} \tag{19}$$

and M and N are functions of the Péclet number

$$M(\mathscr{P}) = \frac{1}{1+\mathscr{P}} \tag{20}$$

$$N(\mathscr{P}) = \frac{1-\phi}{\mathscr{P}-\phi+\phi\mathscr{P}} - \frac{1}{\phi} \tag{21}$$

where ϕ is the Ivantsov function

$$\phi = \mathscr{P}\exp(\mathscr{P})E_1(\mathscr{P}) \tag{22}$$

and E_1 is the exponential integral

$$E_1(\xi) = \int_\xi^\infty \frac{e^{\xi'}}{\xi'}\,d\xi'. \tag{23}$$

As mentioned in the previous section, $\kappa = 0$, so that ΔT_0 goes to zero and the criterion defined in equation (14) is not applicable in the present format. However, based on the definition of ΔT_0 [13], it is possible to write

$$\Delta T_0 = mC_\infty\frac{(\kappa-1)}{\kappa} \quad \text{or} \quad \kappa\Delta T_0 = mC_\infty(\kappa-1). \tag{24}$$

Therefore, as $\kappa \to 0$, the product $\kappa\Delta T_0$ has a finite value

$$\kappa\Delta T_0 = mC_\infty. \tag{25}$$

The term $\kappa\Delta T_0$ is replaced by mC_∞ in all the equations and, from the phase diagram, $\kappa\Delta C_0$ may also be set equivalent to C_∞. Equations (13), (14) and (25) are combined to yield

$$\frac{\Delta T}{mC_\infty} = \left(\frac{\phi}{1-\phi(1-\kappa)}\right)\left(1 + \frac{1}{2}\mathscr{G}N(\mathscr{P}) + \frac{2\mathscr{A}}{\mathscr{P}^2}f(\mathscr{P})\right). \tag{26}$$

Equations (13) and (26) were applied to compute the solute concentrations and the tip temperatures for 12 different states during a freezing trial and were compared with the corresponding measured temperatures and concentrations. Values of the thermal diffusivity and heat conductivity for the solid and liquid phases, as well as the heat capacity, latent heat, surface free energy, the coefficient of mass diffusivity, and other relevant physical properties applied in this analysis are given in ref. [1]. In performing the computations it was not fully apparent from Trivedi [13] which values of the liquidus curve m and the far-field solute concentration C_∞ were appropriate to use in the equations. Also, the value of the effective temperature gradient at the interface, G_{if}, which occurs in equation (18), is determined from equation (19). Here, G_l and G_s are defined as far-field temperature gradients in the liquid and solid phases, respectively, although the meaning of far field is not defined explicitly in the original work [13]. An important consideration in evaluating the experimental data for comparison with the model stability criterion is that for a system of finite dimensions, such as the microscope freezing stage, C_∞ may change with time as there is an accumulation of solute over a range comparable with the length of the stage along the direction of interface movement.

Two options were considered for evaluating the value of the liquidus curve slope, m. In one case, the curve was approximated by a line with constant slope over the entire concentration range from pure water to eutectic solution. Alternatively, the slope was determined from phase diagram data [5] at the initial solute concentration, which should nominally be equal to the far-field value. Accordingly, the local slope of the liquidus curve at a concentration of 2.16 wt% is -0.249 K (wt%)$^{-1}$, in comparison with -0.383 K (wt%)$^{-1}$ if the curve is approximated by a linear function over the entire range of solute concentrations from zero to the eutectic.

Given these options for computing the interface parameters for the Trivedi model, four different approaches were investigated and compared with the experimental data. Combinations of the two values of m identified above with two values of C_∞ were applied to the model. C_∞ was determined either as the initial isotonic value prior to the start of freezing or from a local measurement at the far edge of the field of view in the microscope, which was about 100 μm from the forward boundary of the interface. The interface concentration and temperature values obtained by these calculations are presented in Table 2.

Comparison of the solute concentrations from the model and the data and the data temperatures with the model temperatures show that considerably better

Table 2. Comparison of experimental data and the Trivedi criterion according to equations (13) and (27) for dendrite tip stability for values selected from 12 different states during the solidification trial. The calculations were performed for four combinations of far-field solute concentration, C_∞, based on the initial homogeneous isotonic composition or the local value measured in the microscopic field of view, and the slope of the liquidus curve evaluated at the initial solute concentration, $m = 0.25$, or averaged over the entire range of possible concentrations ranging from zero to eutectic, $m = 0.38$

Temperature and concentration data				Trivedi model parameters							
				Solute concentration (wt%)				Interface temperature (°C)			
				$m = 0.25$		$m = 0.38$		$m = 0.25$		$m = 0.38$	
Interface temperature (°C)	Interface velocity (mm s^{-1})	Solute concentration (wt%)	Equivalent temperature (°C)	Undercool ΔT (°C)	Initial	Local	Initial	Local	Initial	Local	Initial	Local
−3.45	9.54×10^{-3}	2.16	−0.53	0.17	2.85	2.85	2.61	2.61	−0.84	−0.84	−0.79	−0.79
−1.65	4.80×10^{-3}	4.15	−1.02	0.22	3.05	4.24	2.74	3.81	−0.93	−1.18	−0.87	−1.08
−1.77	3.53×10^{-3}	4.50	−1.02	0.19	2.91	4.04	2.65	3.68	−0.87	−1.09	−0.82	−1.02
−1.63	2.00×10^{-3}	7.20	−1.70	0.29	3.32	6.14	2.91	5.40	−1.05	−1.73	−0.97	−1.53
−1.86	1.46×10^{-3}	7.50	−1.84	0.51	4.21	7.80	3.50	6.47	−1.46	−2.44	−1.31	−2.05
−2.15	1.18×10^{-3}	8.50	−2.12	0.45	3.98	8.85	3.35	7.44	−1.35	−2.67	−1.22	−2.28
−2.74	8.06×10^{-4}	9.50	−2.42	0.45	3.95	10.96	3.32	9.22	−1.33	−3.28	−1.21	−2.77
−4.92	6.04×10^{-3}	9.50	−2.42	0.13	2.66	11.10	2.49	10.38	−0.76	−3.01	−7.24	−2.79
−5.15	5.44×10^{-3}	7.50	−1.84	0.18	2.96	6.62	2.62	6.06	−0.85	−1.76	−0.80	−1.60
−4.94	2.14×10^{-3}	8.50	−2.12	0.25	3.15	7.29	2.81	6.49	−0.98	−2.03	−0.91	−1.80
−4.79	2.14×10^{-3}	8.70	−2.18	0.34	3.54	9.83	3.06	8.49	−1.51	−2.84	−1.06	−2.46
−4.93	1.00×10^{-3}	9.00	−2.26	0.61	4.59	17.00	3.61	13.85	−1.64	−5.53	−1.45	−4.38

agreement is produced by basing the calculations on the solute concentration evaluated at a distant position within the microscopic field of view rather than the initial homogeneous solution composition prior to the initiation of freezing. The choice of the best value of the liquidus curve slope is not so obvious, and the calculations are not as sensitive to this parameter.

Interface periodicity

Thermal and solute concentration fields at the interface interact to determine, along with the rate of boundary movement, the shape of the solid–liquid interface. The morphologies are classified by the categories of planar, cellular and dendritic with increasing degrees of geometric complexity. Although there are numerous analyses that describe the growth of the solid phase in a steady state with one of the characteristic interface shapes, as described above, there is a paucity of theories to describe the evolution from one morphological domain to another. The self organization of an interface into a specific pattern is a difficult problem of great current interest [26–29]. Although the purpose of the present study was not to acquire data describing the morphological transitions during solidification processes, the experimental trials have afforded a limited perspective on the conditions requisite to the development of new interface shapes. A characteristic of the transition to a more complex interfacial geometry is the development of a periodic pattern of instability, which will eventually issue in a stable cellular or dendritic shape. The periodicity of the developing pattern is manifested into an intercellular of interdendritic spacing, or wavelength, λ. When a planar interface becomes unstable, it assumes undulatory geometry, and, eventually is transformed into a cellular interface. When a cellular interface becomes unstable, it first becomes undulatory at the sides and side branching starts and eventually is transformed into a dendritic interface.

Billia *et al.* [29] have presented a model for the degree of melt supersaturation at a cellular or dendritic tip in terms of thermal, chemical and geometric parameters, including the periodicity λ of the structure

$$\frac{C_t - C_\infty}{C_t(1-\kappa)} = \frac{D_l G_l}{m C_t V(\kappa-1)} + \frac{\pi\rho}{2\lambda} \times \left(\sqrt{\left(1+\frac{4\lambda}{\pi\rho}\right)}-1\right)\left(1-\frac{D_l G_l}{m(\kappa-1)C_t}\right). \quad (27)$$

This model is based on the assumption of uniform thermal conductivities in the solid and liquid phases and negligible latent heat, and it indicates a proportional relationship between the tip radius of curvature, ρ, and the spacing dimension, λ. Alternatively, Flemings [37] has presented a simplified expression derived from the work of Rohatgi and Adams [38], based on negligible supercooling in the intercellular region, relating the same three categories of param-

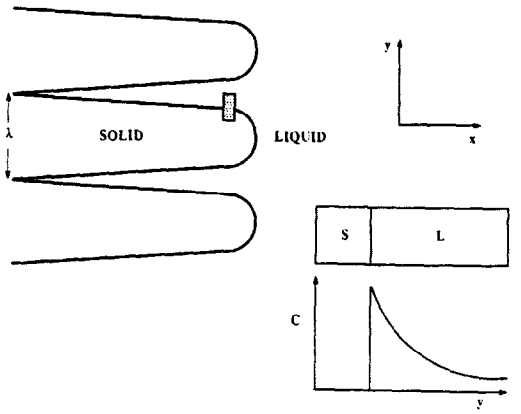

FIG. 11. A simplified geometry of the lateral solute diffusion pattern in the intercellular region.

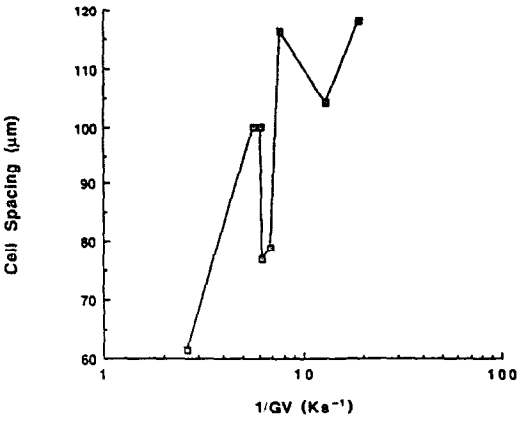

FIG. 12. Experimental values of intercellular spacing measured for a spectrum of local cooling rates, as defined by equation (28).

eters to the spacing between adjacent cellular or dendritic structures

$$\Delta C_L = -\frac{GV\lambda^2}{2mD_l} \tag{28}$$

where ΔC_L is the lateral concentration differential in the intercellular region. The geometry of the system as related to lateral diffusion gradients is depicted in Fig. 11. The cell spacing λ is proportional to the reciprocal of the product of the temperature gradient and the growth velocity, $(GV)^{-1/2}$. Figure 12 shows data for $(GV)^{-1}$ and λ for eight selected states representing a variety of interface conditions.

The magnitude of cell spacing will adjust by side branching to reduce the degree of constitutional supercooling in the melt, giving rise to secondary growth patterns along a vector that is nominally orthogonal to the primary direction of temperature gradient and interface movement. This phenomenon can be described crudely in terms of solute diffusion in the intercellular melt region. A simplified geometry for this process is shown in Fig. 11. Diffusion of solute along the y-axis is described by

$$\frac{\partial C}{\partial t} = D_l \frac{\partial^2 C}{\partial y^2}. \tag{29}$$

It is convenient to nondimensionalize this equation according to the following format:

$$\tau = t\frac{V}{\Lambda} \tag{30}$$

$$\mathscr{C} = \frac{C}{C_\infty} \tag{31}$$

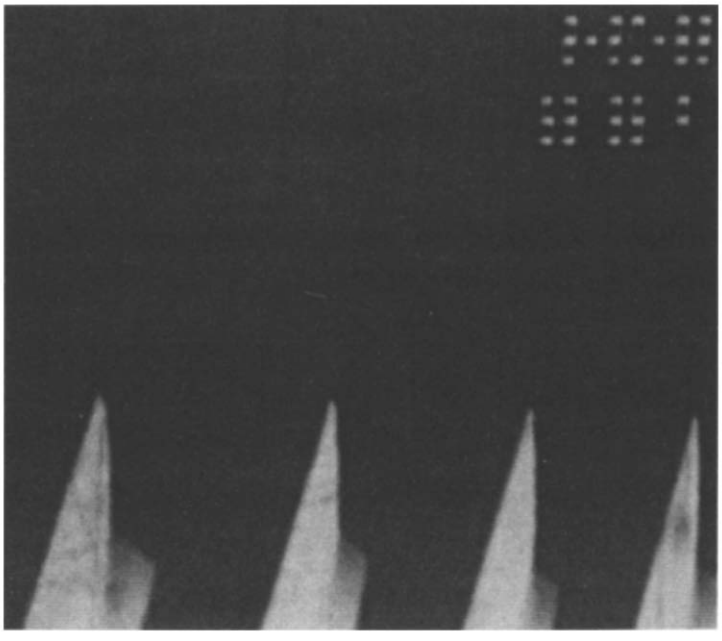

FIG. 13. The onset of side branching from a cellular interface under conditions for which the cell spacing is about one half the mixing length defined in equation (33).

$$y = \frac{y}{\Lambda} \tag{32}$$

where τ, $\mathscr{C}$ and y are dimensionless time, solute concentration and position, respectively, and Λ is a diffusive mixing length defined by

$$\Lambda = \frac{D}{V}. \tag{33}$$

The diffusion equation then becomes

$$\frac{\partial \mathscr{C}}{\partial \tau} = \frac{\partial^2 \mathscr{C}}{\partial y^2}. \tag{34}$$

When the cell spacing is larger than 2Λ, there exists a composition gradient which may establish a significant degree of constitutional supercooling. Figure 13 illustrated the onset of a side growth phenomenon. For this state the local velocity of the interface was 0.0054 mm s^{-1}, and the cell spacing was 129 μm, which is about half of the mixing length value calculated from the above analysis. Thus, a secondary growth pattern resulted on the interface.

CONCLUSION

Computer based densitometric analysis has been employed as an effective tool for determining the microscopic interface morphology and two-dimensional solute concentration field for solidifying binary solutions having a significant absorption coefficient within the visible spectrum of light. Two interface stability theories, namely M–S for planar interfaces and Trivedi for cellular interfaces, were applied and results showed good agreement with experiments for planar interface. Agreement between predictions of the Trivedi model and the results of thermal and concentration data analysis indicates the efficiency of this method as a predictive tool.

Acknowledgement—This research was sponsored by the National Science Foundation under Grant Nos. MEA-8023267 and CBT-8713600.

REFERENCES

1. S. Kourosh, M. E. Crawford and K. R. Diller, Microscopic study of coupled heat and mass transport during unidirectional solidification of binary solutions—I. Thermal analysis, *Int. J. Heat Mass Transfer* **33**, 29–37 (1990).
2. S. Kourosh and K. R. Diller, A unidirectional temperature gradient stage for solidification in aqueous solutions, *J. Microscopy* **135**, 39–48 (1984).
3. S. Kourosh, Ph.D. thesis, The University of Texas at Austin (1983).
4. Ch. Körber, M. W. Scheiwe and K. Wollhöver, Solute polarization during planar freezing of aqueous salt solutions, *Int. J. Heat Mass Transfer* **26**, 1241–1253 (1983).
5. J. C. White and R. R. Miller, Densities and freezing points of sodium permanganate solutions, *J. Am. Chem. Soc.* **75**, 3282–3283 (1953).
6. Ch. Körber and M. W. Scheiwe, Observation of the non-planar freezing of aqueous salt solutions, *J. Crystal Growth* **61**, 307–318 (1983).
7. C. D. Evans and K. R. Diller, A programmable, microprocessor controlled temperature stage for burn and freezing studies in the microcirculation, *Microvas. Res.* **24**, 214–225 (1982).
8. L. Pauling, *General Chemistry* (2nd Edn). Freeman, San Francisco, California (1959).
9. B. Vemuri, K. R. Diller, L. S. Davis and J. K. Aggarwal, Image analysis of solid–liquid interface morphology in freezing solutions, *Pattern Recognition* **16**, 51–61 (1983).
10. M. E. Glicksman, R. J. Schaefer and J. D. Ayers, High-confidence measurement of solid/liquid surface energy in a pure material, *Phil. Mag.* **32**, 725–743 (1975).
11. G. P. Ivantsov, *Dokl. Akad. Nauk S.S.S.R.* **58**, 567 (1947).
12. R. Trivedi, G. Franke and R. Lacmann, Effects of interface kinetics on the growth rate of dendrites, *J. Crystal Growth* **47**, 389–396 (1979).
13. R. Trivedi, Theory of dendritic growth during the directional solidification of binary alloys, *J. Crystal Growth* **49**, 219–232 (1980).
14. G. B. McFadden and S. R. Coriell, Nonplanar interface morphologies during unidirectional solidification of a binary alloy, *Physica* **12D**, 253–261 (1984).
15. K. Somboonsuk and R. Trivedi, Dynamical studies of dendritic growth, *Acta Metall.* **33**, 1051–1060 (1985).
16. W. W. Mullins and R. F. Sekerka, Morphological stability of a particle growing by diffusion or heat flow, *J. Appl. Phys.* **34**, 323–329 (1963).
17. W. W. Mullins and R. F. Sekerka, Stability of a planar interface during solidification of a dilute binary alloy, *J. Appl. Phys.* **35**, 444–451 (1964).
18. R. F. Sekerka, A stability function for explicit evaluation of the Mullins–Sekerka interface stability criterion, *J. Appl. Phys.* **36**, 264 268 (1965).
19. J. S. Langer and H. Müller-Krumbhaar, Theory of dendritic growth—I. Elements of a stability analysis, *Acta Metall.* **26**, 1681–1687 (1978).
20. S. R. Coriell and R. F. Sekerka, The effect of the anisotropy of surface tension and interface kinetics on morphological stability, *J. Crystal Growth* **34**, 157–163 (1976).
21. G. W. Young, S. H. Davis and K. Brattkus, Anisotropic interface kinetics and tilted cells in unidirectional solidification, *J. Crystal Growth* **83**, 560–571 (1987).
22. R. Trivedi, Theory of dendritic growth under rapid solidification conditions, *J. Crystal Growth* **73**, 289–303 (1985).
23. V. Laxmann, Dendritic solidification in a binary alloy melt: comparison of theory and experiment, *J. Crystal Growth* **83**, 391–402 (1987).
24. V. Laxmann, Dendritic solidification—I. Analysis of current theories and models, *Acta Metall.* **33**, 1023–1035 (1985).
25. V. Laxmann, Dendritic solidification—II. A model for dendritic growth under an imposed thermal gradient, *Acta Metall.* **33**, 1037–1049 (1985).
26. J. S. Langer, Instabilities and pattern formation in crystallization, *Rev. Mod. Phys.* **52**, 1–28 (1980).
27. E. Ben-Jacob, N. Goldenfeld, J. S. Langer and G. Schön, Boundary-layer model for pattern formation in solidification, *Phys. Rev. A* **29**, 330–340 (1984).
28. R. Trivedi and K. Somboonsuk, Pattern formation during the directional solidification of binary systems, *Acta Metall.* **33**, 1061–1068 (1985).
29. B. Billia, H. Jamgotchian and L. Capella, Pattern selection during directional solidification, *J. Crystal Growth* **82**, 747–756 (1987).
30. S. R. Coriell, R. F. Boisvert, R. G. Rehm and R. F. Sekerka, Lateral solute segregation during unidirectional solidification of a binary alloy with a curved solid–liquid interface, *J. Crystal Growth* **54**, 167–175 (1981).
31. J. P. van der Eerden and H. Müller-Krumbhaar, Side-

branch-spectrum for a dendrite-model in three dimensions, *Acta Metall.* **34**, 839–847 (1986).
32. J. S. Langer and H. Müller-Krumbhaar, Theory of dendritic growth—II. Instabilities in the limit of vanishing surface tension, *Acta Metall.* **26**, 1689–1695 (1978).
33. J. S. Langer and H. Müller-Krumbhaar, Theory of dendritic growth—III. Effects of surface tension, *Acta Metall.* **26**, 1697–1708 (1978).
34. T. F. Bower, H. D. Brody and M. C. Flemings, Measurements of solute redistribution in dendritic solidification, *Trans. AIME* **236**, 624–634 (1966).
35. M. G. O'Callaghan and E. G. Cravalho, An analysis of the heat and solute transport during solidification of an aqueous binary solution—I. Basal plane region, *Int. J. Heat Mass Transfer* **25**, 553–562 (1982).
36. M. G. O'Callaghan and E. G. Cravalho, An analysis of the heat and solute transport during solidification of an aqueous binary solution—II. Dendrite tip region, *Int. J. Heat Mass Transfer* **25**, 563–573 (1982).
37. M. C. Flemings, *Solidification Processing*. McGraw-Hill, New York (1974).
38. P. K. Rohatgi and C. M. Adams, Dendritic solidification of aluminum–copper alloys, *Trans. AIME* **239**, 1737–1746 (1967).

ETUDE MICROSCOPIQUE DU TRANSFERT COUPLE DE CHALEUR ET DE MASSE PENDANT LA SOLIDIFICATION UNIDIRECTIONNELLE DE SOLUTIONS BINAIRES—II. ANALYSE DU TRANSFERT DE MASSE

Résumé—Une étude expérimentale du transfert couplé de chaleur et de masse est conduite pour la solidification unidirectionnelle d'une solution binaire avec exclusion de soluté. On rapporte les mesures à l'échelle microscopique du champ bidimensionnel de concentration en soluté pour un protocole de gel qui conduit à une morphologie d'interface de phase cellulaire uniforme. L'analyse densitométrique est utilisée pour évaluer les profils spatio-temporels de concentration de soluté, à la fois pour l'espace intercellulaire et à l'interface mobile liquide–solide suivant les vecteurs avant et latéraux. En relation avec des mesures simultanées du champ de température présentées dans un autre texte, on évalue l'importance du sous-refroidissement constitutionnel et on compare avec des modèles de stabilité d'interface disponibles dans la bibliographie courante.

MIKROSKOPISCHE UNTERSUCHUNG DES GEKOPPELTEN WÄRME- UND STOFFTRANSPORTS BEI DER GERICHTETEN ERSTARRUNG BINÄRER LÖSUNGEN—II. UNTERSUCHUNG DES STOFFTRANSPORTS

Zusammenfassung—Der gekoppelte Wärme- und Stofftransport bei der gerichteten Erstarrung einer binären Lösung wird experimentell untersucht. Diese Abhandlung berichtet über Messungen des zweidimensionalen Konzentrationsfeldes der Lösung im mikroskopischen Maßstab für einen Erstarrungsvorgang, bei dem sich eine Zellstruktur mit gleichmäßigen Phasengrenzen ergibt. Unter Verwendung densitometrischer Verfahren werden räumliche und zeitliche Konzentrationsprofile bestimmt, und zwar für den Zellenzwischenraum und für das Gebiet vor der vorrückenden flüssig–festen Phasengrenze. Zusammen mit dem gleichzeitig gemessenen Temperaturfeld, über das in einer zweiten Arbeit berichtet wird, wird die Unterkühlung abgeschätzt und mit den in der zugänglichen Literatur vorhandenen Modellen für die Grenzflächenstabilität verglichen.

МИКРОСКОПИЧЕСКОЕ ИССЛЕДОВАНИЕ СВЯЗАННОГО ТЕПЛО- И МАССОПЕРЕНОСА В ПРОЦЕССЕ НАПРАВЛЕННОГО ЗАТВЕРДЕВАНИЯ БИНАРНЫХ РАСТВОРОВ—II. АНАЛИЗ МАССОПЕРЕНОСА

Аннотация—В предыдущей статье экспериментально исследован связанный тепло- и массоперенос в процессе направленного затвердевания бинарного раствора без учета поведения растворенного вещества. В данной работе представлены измерения в микроскопическом масштабе двумерного поля концентрации растворенного вещества при анализе процесса замораживания. На основе денситометрического анализа в пространственных и временных координатах оцениваются концентрационные профили растворенного вещества как в объеме, так и у границы раздела жидкой и твердой фаз. Наряду с одновременными измерениями температурного поля, представленными в предыдущей статье, определяется переохлаждение смеси, сопоставляемое с результатами моделей межфазной устойчивости, описанных в современной литературе.